

Chemical ordering in Cr₃Al and relation to semiconducting behavior

Z. Boekelheide,^{1,2,*} D. A. Stewart,³ and F. Hellman^{1,2}

¹*Department of Physics, University of California, Berkeley, Berkeley, California 94720, USA*

²*Materials Sciences Division, Lawrence Berkeley National Laboratory, Berkeley, California 94720, USA*

³*Cornell Nanoscale Facility, Cornell University, Ithaca, New York 14853, USA*

(Received 16 February 2012; published 15 August 2012)

Cr₃Al shows semiconductor-like behavior which has been attributed to a combination of antiferromagnetism and chemical ordering of the Cr and Al atoms on the bcc sublattice. This article presents a detailed theoretical and experimental study of the chemical ordering in Cr₃Al. Using density functional theory within the Korringa-Kohn-Rostoker (KKR) formalism, we consider five possible structures with the Cr₃Al stoichiometry: a bcc solid solution, two-phase C11_b Cr₂Al + Cr, off-stoichiometric C11_b Cr₃Al, D0₃ Cr₃Al, and X-phase Cr₃Al. The calculations show that the chemically ordered, rhombohedrally distorted X-phase structure has the lowest energy of those considered and should, therefore, be the ground state found in nature, while the D0₃ structure has the highest energy and should not occur. While KKR calculations of the X phase indicate a pseudogap in the density of states, additional calculations using a full potential linear muffin-tin orbital approach and a plane-wave technique show a narrow band gap. Experimentally, thin films of Cr_{1-x}Al_x were grown and the concentration, growth temperature, and substrate were varied systematically. The peak resistivity (2400 μΩ-cm) is found for films with $x = 0.25$, grown epitaxially on a 300 °C MgO substrate. At this x , a transition between nonmetallic and metallic behavior occurs at a growth temperature of about 400 °C, which is accompanied by a change in chemical ordering from X phase to C11_b Cr₃Al. These results clarify the range of possible structures for Cr₃Al and the relationship between chemical ordering and electronic transport behavior.

DOI: [10.1103/PhysRevB.86.085120](https://doi.org/10.1103/PhysRevB.86.085120)

PACS number(s): 71.20.Lp, 61.66.Fn, 72.80.Ga, 71.28.+d

I. INTRODUCTION

Alloys and compounds made of metallic elements are generally expected to be metallic, and indeed most are. However, some such compounds are semiconducting or semimetallic, such as RuAl₂ and Fe₂VAl.¹ In theory, any compound with an even number of valence electrons in the primitive unit cell can be semiconducting because the electrons can completely fill the valence band. Transition metals usually have several overlapping *d*-like bands at the Fermi energy (E_F), so even in compounds with an even number of electrons typically several bands are partially filled. For an intermetallic compound to be semiconducting, hybridization must shift the bands in a fortuitous way, leaving a gap at E_F .

When intermetallic compounds do have a gap at E_F , they are the subject of significant study. The gap can be exploited for applications, for example, intermetallic semiconductors are attractive for thermoelectric devices due to their typically small gaps and large Seebeck coefficients (e.g., ZrNiSn).^{2,3} In ferro- or ferrimagnetic compounds, the gap is generally asymmetric with spin; if a gap occurs at E_F for one spin but not the other, the result is a half-metal (e.g., Co₂MnAl).⁴ Half-metals are important for spintronics applications such as spin transistors and nonvolatile logic.

Cr_{1-x}Al_x, with $x = 0.15$ – 0.26 , shows semiconductor-like electronic behavior. Our photoemission study showed a narrow gap or pseudogap in a Cr_{0.80}Al_{0.20} thin film.⁵ A maximum resistivity of 3600 μΩ-cm occurs in bulk, with a negative temperature coefficient of resistivity.^{6,7} In addition, a large Hall coefficient and a small electronic specific heat are observed;^{6,8} these are all hallmarks of semiconducting behavior. The maximum resistivity and Hall coefficient and minimum electronic specific heat all occur around $x = 0.25$. Cr_{1-x}Al_x is antiferromagnetic for $x = 0$ – 0.50 , with a plateau in the

magnetic susceptibility also at $x = 0.25$.^{9–11} This suggests that an ordered Cr₃Al structure may be responsible.

The nature of any gap in Cr₃Al is currently of interest. The experimental results in the literature are suggestive of either a semimetal or a degenerate semiconductor. A full, semiconducting gap might suggest further study of Cr₃Al as a potential thermoelectric material. In addition, recent theoretical work has predicted that Cr₃Al with a binary Heusler (D0₃) ordering is almost completely spin polarized and that Mn-doped D0₃ Cr₃Al would behave as a true half-metal with applications in spintronics.¹² While no evidence of D0₃ ordering has been shown in Cr₃Al, the Cr-Al phase diagram is not well established. Thus, a study of the nature of a gap in Cr₃Al and how it is affected by chemical ordering is warranted.

Recent work by our group showed that both antiferromagnetism and chemical ordering are necessary for the semiconductor-like behavior in Cr_{1-x}Al_x to occur. Two film samples were presented, both antiferromagnetic, but with different electronic properties. The films were grown at different temperatures so that one was metallic and one nonmetallic, attributed to differences in chemical ordering of Cr and Al on the bcc sublattice.¹³ The current paper explores the issue of chemical ordering in Cr₃Al more deeply, with density functional theoretical calculations considering five possible structures with the Cr₃Al stoichiometry and a systematic study of thin-film growth of Cr_{1-x}Al_x, varying concentration, growth temperature, and substrate. Our results support the proposed Cr-Al phase diagram and show that D0₃ ordering is unlikely to occur. We also show how the antiferromagnetic X-phase structure explains the observed electronic transport behavior and find that a perfect crystal of X-phase Cr₃Al should have a complete band gap.

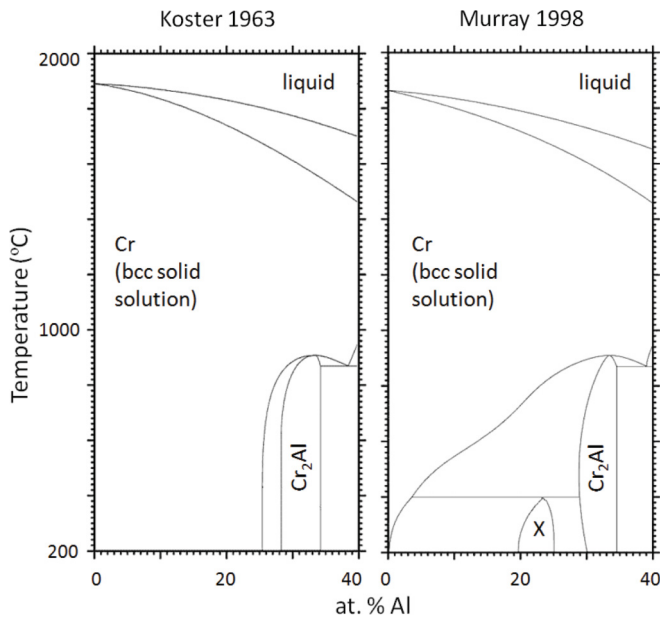


FIG. 1. Binary phase diagrams of the $\text{Cr}_{1-x}\text{Al}_x$ system, as shown by Koster *et al.*^{10,50} and Murray.^{15,51} (Adapted with the permission of ASM International. All rights reserved. www.asminternational.org.)

II. BACKGROUND

The structural Cr-Al phase diagram is not clear. Based on x-ray diffraction (XRD), Koster *et al.*¹⁰ created a phase diagram of $\text{Cr}_{1-x}\text{Al}_x$ in 1963. Koster's phase diagram, reproduced in Fig. 1(a), shows a bcc solid solution (α) as the stable phase from $x = 0$ to $x = 0.26$. The C11_b Cr_2Al (β) phase is shown for $x = 0.29$ – 0.34 and a two-phase region is shown between $x = 0.26$ – 0.29 . Koster *et al.* suggested that a Cr_3Al ordered compound may exist due to the nonlinear dependence of magnetic susceptibility on x but found no evidence for it upon XRD and did not include it in the phase diagram.

In 1981, den Broeder *et al.* saw evidence in transmission electron microscopy (TEM) diffraction patterns for an ordered Cr_3Al structure at temperatures below 400°C .¹⁴ They observed additional diffraction spots which could be interpreted as superlattice spots. They proposed an ordered phase, called the X phase, for $x = 0.19$ – 0.26 , with a low 400°C phase boundary. The updated phase diagram, taken from Murray's 1998 phase diagram evaluation, is shown in Fig. 1(b).¹⁵

According to dark-field imaging, the X-phase ordering occurs in small, 1- to 3-nm domains, even within a large bcc crystallite. The roughly 400°C phase boundary was suggested because annealing at temperatures of 400°C or above did not improve the size of the crystallites.¹⁴ Such a low temperature phase boundary can impede long-range order because the low atomic mobility requires extremely long annealing times to achieve ordering. Thus, the X phase observed by den Broeder *et al.* is best described as short- to medium-range order.

Based on first-order diffraction spots, the authors suggested that the X phase was a rhombohedral structure with eight atoms in the unit cell. Because no higher order diffraction spots were observed, they could not be conclusively attributed to a specific structure and thus Cr_3Al and Cr_5Al_3 were both suggested as candidates for the X phase. For the purposes of this work, we

consider the Cr_3Al structure due to the observed anomalous behavior peaking at $x = 0.25$. The X phase is still considered speculative because it has only been observed once.

The proposed phase diagram in Fig. 1(b) shows, for the Cr_3Al composition, three solid phases occurring in different temperature ranges. The X phase is stable below 400°C , the C11_b $\text{Cr}_2\text{Al} + \text{bcc Cr}$ two-phase system is stable from 400° to 800°C , and the bcc solid solution is stable above 800°C until melting.

Another structure worthy of consideration is the binary Heusler (D0_3) structure. The Heusler structure is commonly seen for compounds with a transition metal:main group element ratio of 3:1. Heusler compounds have a standard electronic band structure with a band gap between the twelfth and the thirteenth bands, so that compounds with a total number of valence electrons $Z = 24$ are semiconducting or semimetallic (e.g., Fe_2VAl), and many compounds with more or less electrons are predicted to be half-metallic (e.g., Co_2MnAl). The semiconductor-like behavior in Cr_3Al is reminiscent of the behavior in Heusler-structure Fe_2VAl , but cannot be explained by the Heusler structure because $Z = 21$ for Cr_3Al . However, theoretically, Heusler Cr_3Al may be desirable as a potential half-metal.¹² Although D0_3 Cr_3Al does not appear in the currently available Cr-Al phase diagrams, it might be reasonable to expect it to be formed under certain growth conditions.

We explore here the three structures shown in the proposed phase diagram: a bcc solid solution, a C11_b $\text{Cr}_2\text{Al} + \text{bcc Cr}$ two-phase system, and an X-phase Cr_3Al structure. Also included are an off-stoichiometric C11_b Cr_3Al structure, which we see experimentally for films grown at 500 – 600°C (above the proposed X-phase transition temperature), and the common D0_3 structure.

A. bcc Cr

Cr occurs in the bcc structure shown in Fig. 2(a), and all the Cr_3Al structures discussed here have a bcc-like atomic

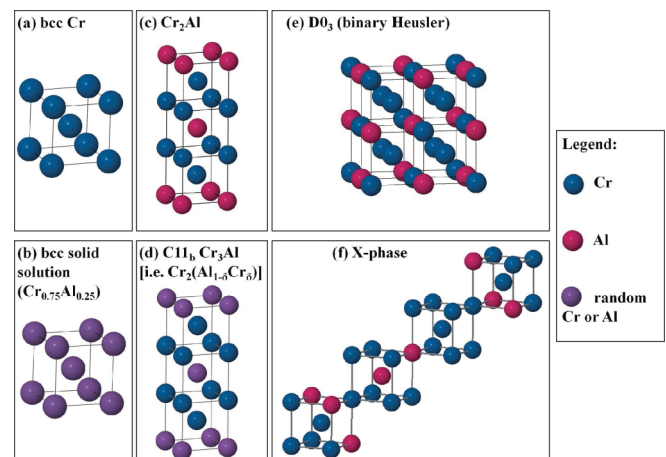


FIG. 2. (Color online) Structures considered in Secs. V and VI. (b) In the bcc solid solution, the atoms are randomly Cr or Al in the ratio $\text{Cr}_{0.75}\text{Al}_{0.25}$. (d) In the off-stoichiometric C11_b Cr_3Al phase, the atoms at the Al sites are randomly Cr or Al in the ratio $\text{Cr}_{0.25}\text{Al}_{0.75}$, for a total stoichiometry of $\text{Cr}_2(\text{Al}_{0.75}\text{Cr}_{0.25})$, or Cr_3Al .

environment, albeit with different types of chemical ordering and, in some cases, slight distortion. The bcc structure has one atom per primitive unit cell. However, when simple antiferromagnetism is considered, there are two atoms per unit cell (one up, cube edge; one down, body center).

B. bcc solid solution Cr_{0.75}Al_{0.25}

This structure occurs when Al is added to the bcc Cr system and the Al atoms are placed randomly on the lattice sites. The lattice constant is increased slightly because the atomic radius of Al is larger than that of Cr.⁶ This structure is shown in Fig. 2(b).

C. C11_b Cr₂Al

The C11_b Cr₂Al structure is layered along the bcc (001) planes, so that there are alternating layers (Cr, Cr, Al, Cr, Cr, Al, etc.). Thus the unit cell consists of essentially three bcc unit cells, with six atoms per Cr₂Al unit cell. The layering creates a 4% tetragonal distortion.¹⁰ The C11_b Cr₂Al structure is shown in Fig. 2(c).

The proposed phase diagram only shows single-phase C11_b Cr₂Al for about $x = 0.29$ – 0.34 , so for the Cr₃Al stoichiometry, the two-phase C11_b Cr₂Al + bcc Cr structure is considered. C11_b Cr₂Al also displays simple antiferromagnetism.¹⁶

D. C11_b Cr₃Al

Although single-phase C11_b does not appear for the Cr₃Al stoichiometry in the phase diagram, we observe it experimentally. In this case, the C11_b Cr₂Al structure has the additional Cr atoms substituted randomly onto Al sites (i.e., Cr₂(Al_{1- δ} Cr _{δ}), where $\delta = 0.25$ for the Cr₃Al stoichiometry). The C11_b Cr₃Al structure is shown in Fig. 2(d).

E. D0₃ Cr₃Al

We include the binary Heusler structure (D0₃), although it does not appear in the phase diagram, because so many other bcc transition metal-Al alloys take this form. The full Heuslers have an A₂BD structure, where A and B are transition metals and D is an *sp* element. The atoms occupy the sites of a bcc lattice with an L2₁ ordering. For binary Heuslers (A₃D), atom A occupies two distinct sites and can be thought of as A(I)₂A(II)D (e.g., Fe₃Si).

The D0₃ ordering can be seen as four interpenetrating fcc lattices, thus the primitive unit cell contains four atoms. In Fig. 2(e), Cr(I) occupy the body centers of the cube, while Cr(II) and Al occupy alternating cube edges. Cr₃Al in the D0₃ structure has been considered theoretically before and has been calculated to be ferrimagnetic due to antiferromagnetic coupling between the Cr(I) and the Cr(II) sites with different magnitudes of moment.¹²

F. X-phase Cr₃Al

The proposed X phase is a chemically ordered, rhombohedrally distorted phase based on the bcc structure.¹⁴ The primitive unit cell is a rhomboid containing eight atoms along the bcc [111] direction: six Cr atoms followed by two Al atoms. The primitive lattice vectors are [211], [121], and [112] in the

bcc coordinates. The space group for this structure is R $\bar{3}m$. The rhombohedral unit cell appears in Fig. 2(f).

This structure has not been widely observed or studied. Thus, there is no Strukturbericht designation or accepted parent compound for it. We continue to call it the X phase for the bulk of this paper.

III. EXPERIMENTAL METHODS

Most previous studies of Cr-Al alloys have used bulk samples, although a few studies have focused on the potential applications of Cr-Al thin films as the antiferromagnetic layers in exchange-biased multilayer systems^{17–19} and as thin-film resistors.²⁰ In contrast to bulk sample growth, thin-film growth often stabilizes nonequilibrium crystal structures, for example, through quenching of films grown at high temperatures, restriction of lattice parameters due to the substrate, and surface energy effects. We have used thin-film growth techniques in order to study the effect of structure on the transport properties of Cr-Al.

Thin films of Cr_{1-x}Al_x, with a thickness of ~ 400 Å, were grown on MgO(001) and *a*-SiO₂/Si substrates to achieve epitaxial and polycrystalline growth, respectively, by co-deposition of Cr from an e-beam source and Al from an effusion cell at a rate of 0.4 Å/s and a base pressure of 5×10^{-9} Torr. One series was grown at a substrate temperature of 300 °C, with the Al concentration (x) varied. Another series of films was grown at a fixed Al concentration ($x = 0.24$) but a varied substrate temperature, from 200 ° to 600 °C. We did not attempt growth above 600 °C due to the potential loss of Al above its melting temperature (660 °C).

Cr(001) is known to grow epitaxially on MgO(001).^{21,22} The MgO lattice constant is 4.211 Å, or about $\sqrt{2}$ larger than that of Cr. The Cr lattice grows 45° rotated compared to the substrate ([001]Cr || [110]MgO). For pure Cr, the lattice mismatch for this epitaxial relation is 3.9%, while the addition of Al increases the lattice constant and improves the mismatch to approximately 1% at the Cr₃Al stoichiometry. Epitaxy was verified *in situ* by reflection high-energy electron diffraction (RHEED), which showed a streaky pattern and *ex situ* by XRD, which showed fourfold symmetry of the (011) peak in an azimuthal scan at 45° from normal. In addition, only the bcc (001) orientation is seen in a $\theta - 2\theta$ scan [see Fig. 3(a)]. The films grown on *a*-SiO₂/Si are polycrystalline, as the *a*-SiO₂ layer provides an amorphous surface for growth. In addition, it acts as a diffusion barrier to prevent silicide formation at the interface.

The films were patterned lithographically to form a defined geometry for the resistivity measurements. The resistivity was measured from 2 to 300 K by a four-probe technique, averaging forward and reverse currents to avoid thermal voltages. In addition, the *I-V* curve was confirmed to be linear for each sample.

IV. EXPERIMENTAL RESULTS

The 2 K resistivity of films as a function of Al concentration is shown in Fig. 4. It shows a clear peak at 25 at% Al, similar to the results for bulk samples.^{6,7} In addition, the temperature dependence of the resistivity is shown in the inset for 23 at% Al

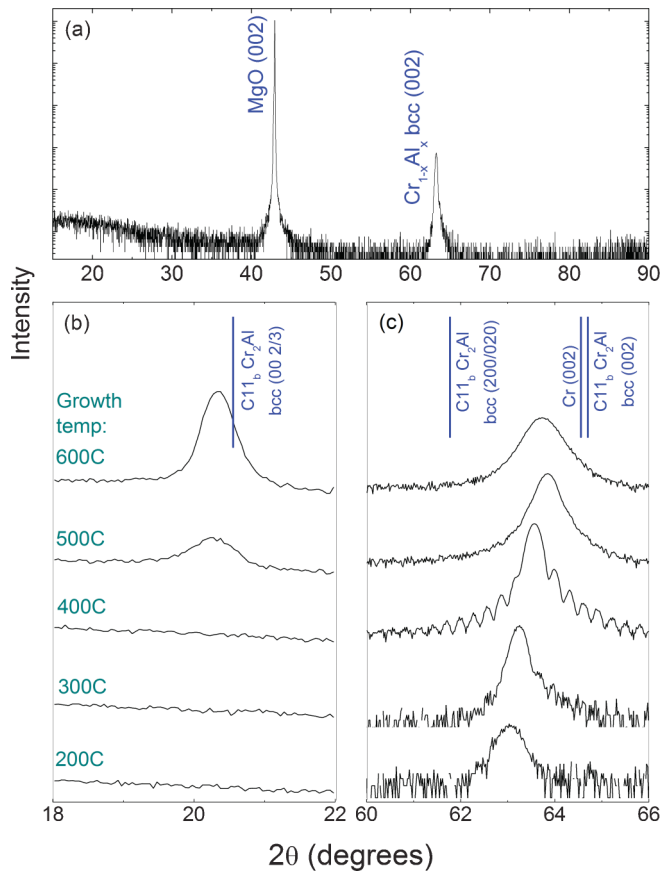


FIG. 3. (Color online) XRD of epitaxial $\text{Cr}_{0.76}\text{Al}_{0.24}$ (a) $\theta - 2\theta$ survey of films grown at 300°C . (b) $(0\ 0\ \frac{2}{3})$ peak of films grown at several temperatures. (c) $(0\ 0\ 2)$ peak of films for several growth temperatures. Note that some of the (002) peaks have sufficient intensity to show thickness oscillations, corresponding to the approximately 400-\AA thickness of the films.

for both an epitaxial and a polycrystalline film. The negative temperature dependence is decidedly nonmetallic and similar to what has been seen in bulk.

However, there are significant differences between the thin films and the bulk. In the bulk, the metallic Cr_2Al phase begins to precipitate at 26 at% Al, leading to a steep drop in resistivity above 25 at%. Thus, it could not be determined previously whether the peak $\rho(2\text{ K})$ at 25 at% Al was related to the formation of a distinct Cr_3Al phase or whether a peak in $\rho(2\text{ K})$ occurred at 25 at% Al simply due to an accidental confluence of factors: slowly increasing resistivity with x , combined with a sudden drop at 26 at% Al due to precipitation of metallic Cr_2Al .

In contrast to the bulk, none of our films shown in Fig. 4 (grown at 300°C) show evidence of the Cr_2Al phase in XRD, up to 37 at% Al. The resistivity of our films still peaks at 25 at% Al, but the decrease in resistivity for concentrations above 25 at% is much more gradual in the films than in the bulk, still displaying nonmetallic behavior up to about 37 at% Al. This suggests that the peak in $\rho(2\text{ K})$ at 25 at% Al is not related to precipitation of the Cr_2Al phase but, rather, to an ordered Cr_3Al structure.

The magnitude of the peak resistivity reaches about $2400\ \mu\Omega\text{-cm}$ in the films but as high as $3600\ \mu\Omega\text{-cm}$ in the

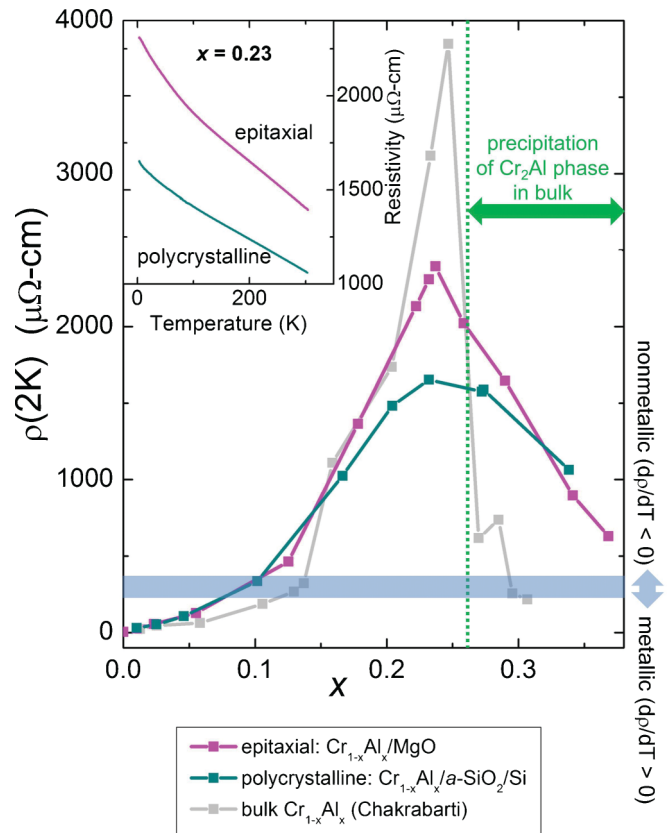


FIG. 4. (Color online) Resistivity of $\text{Cr}_{1-x}\text{Al}_x$ thin films vs x at 2 K . All films shown here were grown at 300°C . Bulk data from Ref. 6. Error bars are smaller than the symbol size. Inset: Resistivity of $\text{Cr}_{0.77}\text{Al}_{0.23}$ vs temperature.

bulk.^{6,7} This difference is unexplained as of yet but could be due to a different quality of Cr_3Al formation in the samples or due to strain in the films, from either thermal expansion or substrate mismatch effects.

Figure 4 also shows a noticeable effect of the substrate. The polycrystalline films, grown on $a\text{-SiO}_2/\text{Si}$, have a significantly lower resistivity than their epitaxial counterparts. This is clearly shown in the inset in Fig. 4, which compares two films grown at the same time on different substrates. The polycrystalline films have not only a lower 2 K resistivity, but also a weaker temperature dependence of resistivity.

This result is surprising at the outset, given that the primary quantities leading to the resistivity are the scattering time τ and the number of carriers n . The addition of grain boundaries adds scattering centers and should decrease τ , leading to higher resistivity. The lower resistivity of the polycrystalline samples implies an opposing, and larger, effect on n , further suggesting that the anomalous transport behavior in this material is due to a band structure effect.

A second series of samples, with 24 at% Al, varied the growth temperature between 200° and 600°C . The 2 K resistivity is shown in Fig. 5. The results show a transition from clearly nonmetallic behavior at lower growth temperatures to more metallic behavior at the highest growth temperatures, as seen in the previous study.¹³ These data show the transition around 400°C , aligning with the proposed phase boundary

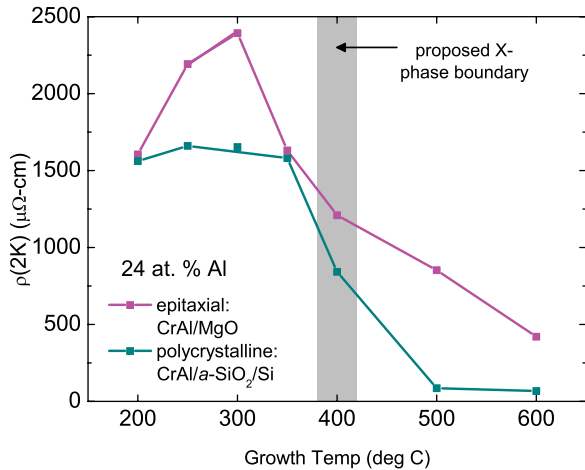


FIG. 5. (Color online) The 2 K resistivity of Cr_{0.76}Al_{0.24} thin films vs growth temperature. Error bars are smaller than the symbol size. The X-phase boundary at 400 °C was proposed by den Broeder *et al.* in Ref. 14.

from X-phase Cr₃Al to metallic C11_b Cr₂Al + Cr (Fig. 1). Indeed, the epitaxial films grown at 500 ° and 600 °C show C11_b superlattice peaks at the bcc (0 0 $\frac{2}{3}$) position,²³ while films grown at low temperature do not, as shown in Fig. 3(b).

The transition from nonmetallic to metallic behavior is much sharper in the polycrystalline films than the epitaxial films. In addition, the high-temperature-grown polycrystalline films are much more metallic than the epitaxial ones. The difference in behavior between the epitaxial and the polycrystalline films is not exactly clear, but one possibility is due to different formation of the C11_b phase in these films.

Although the proposed Cr-Al phase diagram shows a two-phase region of C11_b Cr₂Al + Cr for the Cr₃Al concentration (Fig. 1), our XRD data are indicative of a single-phase off-stoichiometric C11_b Cr₃Al [Cr₂(Al_{1- δ} Cr _{δ})] for the epitaxial films grown at 500 ° and 600 °C. The structure is shown in Fig. 2(d). This is consistent with the findings for the 600 °C-grown thick film in the previous study.¹³ Figure 3(c) shows that the (0 0 2) peak in XRD does not split as it would in the case of two-phase C11_b Cr₂Al + Cr. The position of the (002) peak shifts to the right with increasing growth temperature, due to tetragonal distortion. We also see that *c*, the axis along which ordering occurs, points preferentially in the out of plane direction. Due to the tetragonal distortion of the C11_b structure, the different *a* and *c* lattice constants would also lead to a split diffraction peak if *c* were randomly oriented throughout the film.

The formation of single-phase C11_b Cr₃Al in our epitaxial films, although it does not occur in the phase diagram, is not surprising. Samples grown using vapor deposition techniques often show nonequilibrium structures, due to the kinetics of phase nucleation. In addition, surface energy effects during growth can cause ordering to occur preferentially along a certain direction, which can explain the orientation of the C11_b *c* axis in the out-of-plane direction. Finally, epitaxy may cause one phase to be preferred over another due to a better lattice constant match with the substrate or a preferential orientation due to a constraint on the lattice constant in the in-plane direction.

V. THEORETICAL METHODS

Density functional theory calculations of all structures considered were done using the AKAIKKR code, so that the results for the different structures could be compared directly. AKAIKKR is a full-potential density functional Green's function approach based on the Korringa-Kohn-Rostoker (KKR) multiple-scattering technique.²⁴⁻²⁶ This technique was chosen for its ability to treat site disorder, which was necessary for the bcc solid solution and off-stoichiometric C11_b Cr₃Al structures. Disorder is treated using the coherent potential approximation.^{27,28} The number of irreducible *k* points used for Brillouin-zone integration was between 3009 and 3276 for the different structures. The scalar relativistic approximation was used and the generalized gradient approximation (GGA) was used to approximate the exchange-correlation energy.²⁹

For the X-phase Cr₃Al structure, additional calculations were done in order to better understand the nature of the pseudogap found in the KKR calculations. These calculations were done using a planewave pseudopotential code, QUANTUM ESPRESSO,³⁰ as well as a full potential linear muffin-tin orbital approach (FP-LMTO).³¹ The Perdew-Burke-Erzenhof formulation of the GGA was used to describe exchange and correlation.³² Ultrasoft pseudopotentials were used for all of the plane-wave calculations. For this study, we used the Cr pseudopotential from the study by R. Soulaire *et al.*,³³ which we found to provide better results for bulk Cr compared to other available pseudopotentials in the QUANTUM ESPRESSO distribution, specifically Cr.pbe-sp.van.UPF and Cr.pw91-sp.van.UPF. An energy cutoff of 40 Ryd was used for the plane-wave expansion to describe the wave functions. The charge density and potential were determined using a 400-Ryd energy cutoff. Brillouin-zone sampling was done using a 24 × 24 × 24 Monkhorst-Pack grid. The general parameters (exchange correlation, *k*-point mesh) were identical for the FP-LMTO calculations. Angular momentum channels up to *l* = 3 were included in the FP-LMTO calculations. The tetrahedron approach was used to calculate the density of states (DOS) in the FP-LMTO calculation. The plane-wave pseudopotential DOS calculation used a Methfessel-Paxton smearing energy of 68 meV.

VI. THEORETICAL RESULTS

Because pure Cr is a well-studied system, we compare our calculations for Cr to experiment to verify that we have chosen appropriate parameters. The calculated Cr lattice constant is very close to experiment (2.882 Å calculated, 2.885 Å experimental). In addition, the bulk modulus is extremely close (1.86 Mbar calculated, 1.97 Mbar experimental). Pure Cr has a spin density wave (SDW) incommensurate with the lattice that is computationally difficult. Not only does it require a large unit cell, but also it is, as of yet, not found to be the minimum energy state in current density functional theory calculations.³⁴ For these reasons, we simplify and assume the commensurate SDW (simple antiferromagnetism) for Cr. We obtain a larger magnetic moment than experimentally observed (1.1 μ_B calculated, 0.60 μ_B experiment,⁹ in the commensurate SDW phase). The large calculated Cr moment is consistent

TABLE I. Parameters for the five Cr₃Al structures and Cr, as calculated using the KKR technique and compared to experiment. The $\Delta E/\text{atom}$ is shown relative to the minimum energy structure (X-phase Cr₃Al). The $\text{DOS}(E_F)$ is shown per atom. The $\text{DOS}(E_F)/\text{atom}$ for the two-phase C11_b Cr₂Al + Cr structure is the weighted average of the $\text{DOS}(E_F)/\text{atom}$ of the two structures.

	Lattice constants (Å)	Magnetic state	$\Delta E/\text{atom}$ (eV)	$\text{DOS}(E_F)$ (1/eV)
Cr				
Experiment	$a = b = c = 2.885$ Å	Antiferromagnetic ⁴⁴	–	0.444 ⁸
Calculated	$a = b = c = 2.882$ Å	Antiferromagnetic	–	0.379
Cr ₃ Al				
Experiment	$a = b = c = 2.949$ Å ⁶	Antiferromagnetic ¹¹	–	0.108 ⁸
Calculated				
bcc solid solution				
Cr _{0.75} Al _{0.25}	$a = b = c = 2.948$ Å	Antiferromagnetic	0.042	0.240
C11 _b Cr ₂ Al + bcc Cr				
Cr ₂ Al	$a = b = 3.017$ Å, $c = 2.899$ Å			
Cr	$a = b = c = 2.882$ Å	Antiferromagnetic	0.039	0.192
C11 _b Cr ₃ Al	$a = b = 2.979$, $c = 2.915$ Å	Antiferromagnetic	0.048	0.224
D0 ₃ Cr ₃ Al	$a = b = c = 2.977$ Å	Ferrimagnetic	0.075	0.207
X phase Cr ₃ Al	$a = b = c = 2.941$ Å			
	90.35° rhombohedral distortion	Antiferromagnetic	0.000	0.076

with calculations in the literature and is due to overestimation of the moment by the GGA.³⁴

Table I lists the relevant calculated parameters for the Cr₃Al structures. The second and third columns show the lattice parameters and magnetic state. Both the calculated bcc solid solution and the X phase have similar lattice parameters to experiment. The rhombohedral distortion of the X phase is small, and if it occurred in many small domains, as seen experimentally by den Broeder,¹⁴ the distortion would not be seen in XRD. The Cr₂Al phase, on the other hand, has a significant tetragonal distortion, which is seen experimentally.²³ The D0₃ phase has cubic symmetry, but a significantly larger lattice constant than the experimental value. All of the calculated structures show antiferromagnetic order except D0₃, which shows ferrimagnetism. This is consistent with previous calculations¹² and the well-known Heusler Slater-Pauling behavior.³⁵ Further details of the magnetic configurations, including magnetic moments on the Cr atoms, have been given previously.¹³ Thus, the Cr₃Al experimental data are not consistent with the D0₃ structure.

The total energy per atom, relative to the minimum energy system, is shown in the fourth column in Table I. The X-phase structure has the lowest energy, suggesting that it is the low-temperature stable phase for the Cr₃Al stoichiometry, as suggested in the proposed phase diagram [Fig. 1(b)]. The bcc solid solution, C11_b Cr₂Al + bcc Cr two-phase system, and C11_b Cr₃Al structure have the next lowest energies, consistent with their being stable phases at higher temperatures. Finally, the D0₃ structure has a significantly higher energy.

The bcc solid solution, C11_b Cr₃Al, and the C11_b Cr₂Al + bcc Cr two-phase system have some degree of disorder. This suggests that entropy of mixing drives the transition from the Cr₃Al X phase. The energy difference between the X-phase Cr₃Al structure and the bcc solid solution is about 0.042 eV. In a model including only the entropy of mixing, the order-disorder transition between these two structures should

be about 600 °C, within the range of the transition on the proposed phase diagram. The C11_b systems are more difficult to model because of the lattice distortion and, in the case of the two phase system, the temperature-dependent solubility of Al in Cr and in C11_b Cr₂Al. The D0₃ structure has no more disorder than the X-phase structure and therefore should theoretically never occur in the equilibrium phase diagram based on energy or entropy.

The fifth column in Table I lists the DOS at E_F . It should be noted that because Cr and the Cr-Al alloys have a pseudogap at E_F due to antiferromagnetism, the DOS varies sharply near E_F and the exact value of the $\text{DOS}(E_F)$ depends somewhat on the input parameters of the calculation. The DOS curves have been shown previously.¹³

To compare the calculated values of $\text{DOS}(E_F)$ to the experimental values, we adjust experimental values for the Sommerfeld coefficient (γ) from the literature by the factor $(1 + \lambda)$. We used $\lambda = 0.34$, one of the reported values for Cr. This value was calculated based on the Sommerfeld coefficient from specific heat measurements and a previously accepted value for the $\text{DOS}(E_F)$.^{36–40} This is a fairly typical value for λ in the transition metals, however, reported values for λ in Cr vary.^{41–43} No values of λ have been reported for Cr₃Al.

Our calculated $\text{DOS}(E_F)$ for Cr is lower than the experimental value by 15%, showing the approximate level of error in $\text{DOS}(E_F)$ calculations. X-phase Cr₃Al has the lowest $\text{DOS}(E_F)$ by more than a factor of 2, closest to the experimental value based on the Sommerfeld coefficient for Cr₃Al.

The decreased $\text{DOS}(E_F)$ in X-phase Cr₃Al is due to a semimetallic band structure, as calculated by KKR. The full band structure has been shown previously,¹³ and a closeup of the region around E_F is shown in Fig. 6(e). Figure 6 shows the evolution of the band structure from Cr to Cr₃Al as X-phase ordering and antiferromagnetism are added to the calculation.

Figure 6(a) shows the band structure of pure, nonmagnetic Cr, which is well known.⁴⁴ Figure 6(b) shows how this same

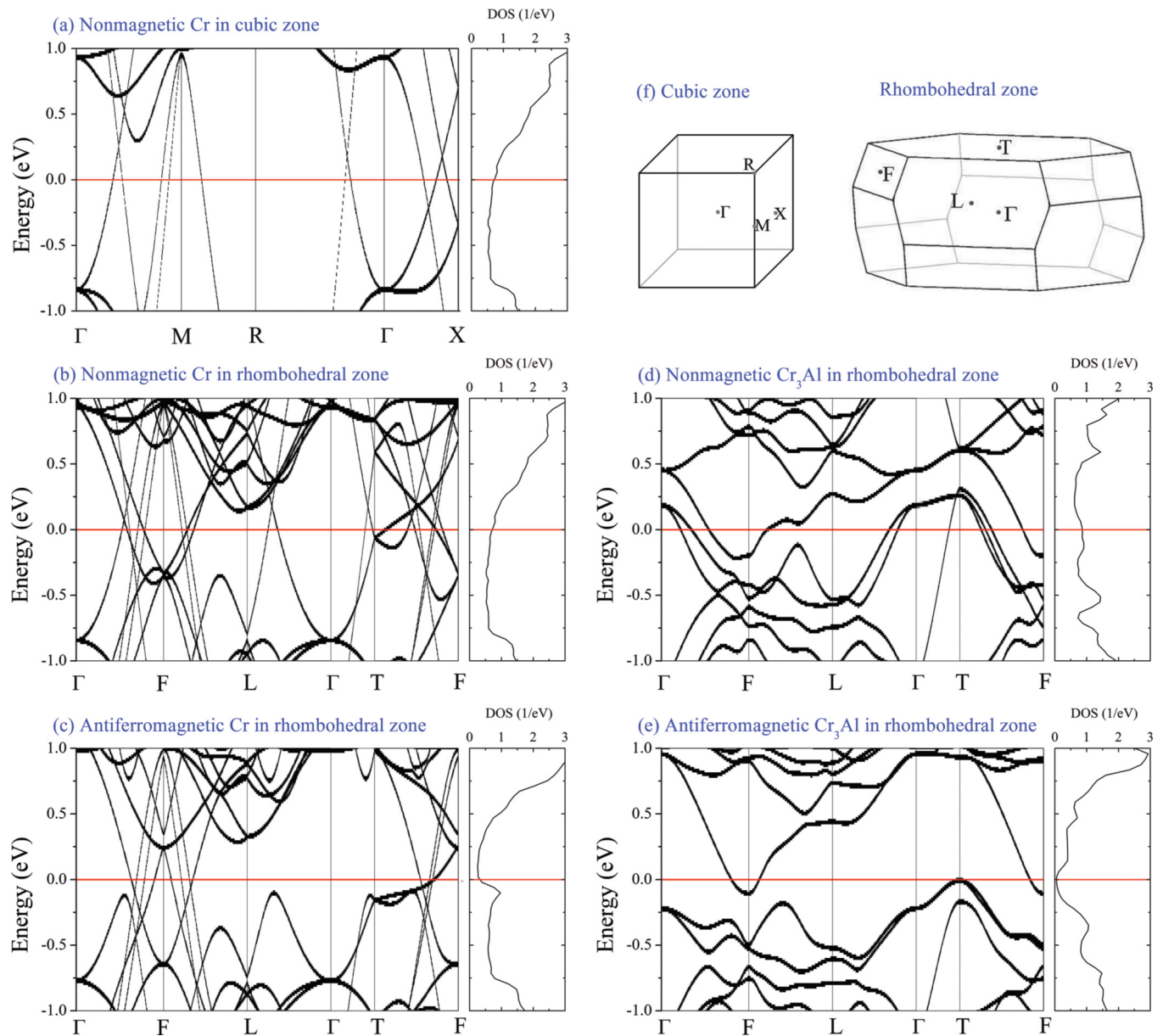


FIG. 6. (Color online) Band structure of Cr and X-phase Cr₃Al, for nonmagnetic and antiferromagnetic cases, calculated using the AKAIKKR technique. (a) Nonmagnetic Cr in the cubic Brillouin zone. (b) Nonmagnetic Cr, (c) antiferromagnetic Cr, (d) nonmagnetic X-phase Cr₃Al, and (e) antiferromagnetic X-phase Cr₃Al, all in the rhombohedral Brillouin zone. (f) Cubic and rhombohedral zones and symmetry points. For reference, point *T* occurs along the bcc [111] axis (the long axis of the rhomboid unit cell in real space).

band structure appears when plotted in the rhombohedral zone used for X-phase Cr₃Al. The DOS, shown to the right of each band structure, is, of course, identical. The antiferromagnetic pseudogap in Cr occurs where the bands cross at Γ -*M* and Γ -*R*, and at one of the crossings in Γ -*X* in the cubic zone. In the rhombohedral zone, this corresponds to gaps at the band crossings at Γ -*L* and Γ -*T* and one of the band crossings at each of Γ -*F* and *T*-*F* [Fig. 6(c)]. This leaves bands still crossing E_F around the *F* point, allowing significant electronic transport and metallic behavior, as expected for Cr.

In nonmagnetic X-phase Cr₃Al, shown in Fig. 6(d), significant band hybridization is seen compared to Cr. The addition of antiferromagnetism, shown in Fig. 6(e), shifts the bands farther apart, leaving bands crossing E_F only slightly at the *F*

and *T* points. This results in a very low DOS and pseudogap, shown in the panel at the right.

The mechanism for the opening of the antiferromagnetic pseudogap is different in Cr and Cr₃Al. In Cr, the antiferromagnetism doubles the unit cell from one atom (bcc) to two atoms (one up, one down, in a simple cubic unit cell). Thus, the band structure in the bcc zone is folded into the cubic zone, and where the bands cross, they open up to form a gap.⁴⁴ In X-phase Cr₃Al, the unit cell is the same for the nonmagnetic and antiferromagnetic case [eight atoms or Cr₆Al₂; see Fig. 2(f)]. The band structure responsible for the pseudogap is already apparent in nonmagnetic X-phase Cr₃Al, although the DOS(E_F) is still quite large. The addition of antiferromagnetism simply pushes the valence and conduction

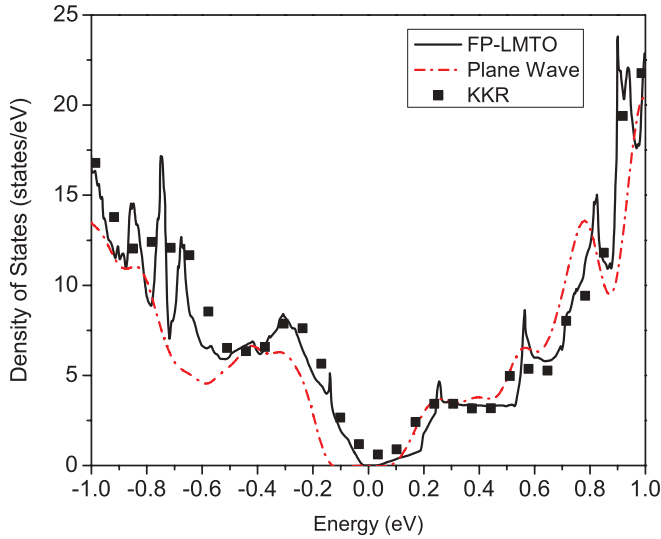


FIG. 7. (Color online) Total density of states for the X phase of Cr_3Al as calculated using the FP-LMTO approach [solid (black) line], plane-wave pseudopotential approach [dash-dotted (red) line], and KKR technique [filled (black) squares]. The energy 0 is set to the Fermi energy in all cases.

bands farther apart, so that the band edges are very close to E_F , and thus lowers the total energy of the system.

Despite the different mechanisms, the result of antiferromagnetism is similar in Cr_3Al and Cr. In both cases, the antiferromagnetism eliminates bands crossing E_F along Γ - F , Γ - L , and Γ - T . The X-phase ordering in Cr_3Al hybridizes the bands so that very few states (if any) appear at E_F around F and T . The combination of antiferromagnetism and X-phase ordering results in the observed semimetallic band structure and very low $\text{DOS}(E_F)$ from KKR calculations.

Density functional calculations often underestimate the band gap in materials, sometimes showing overlapping bands even in materials known to have a full band gap.⁴⁵ The DOS calculated using the KKR approach shows a small finite DOS at the Fermi energy, indicating a semimetal. Since very little experimental or theoretical work has been done on the X phase of Cr_3Al , we also performed complementary calculations using both a plane-wave approach (QUANTUM ESPRESSO) and an FP-LMTO approach.

Figure 7 compares the calculated DOS for the three approaches. It is clear that, overall, the different theoretical approaches are in good agreement and produce similar features in the DOS near the Fermi energy. The QUANTUM ESPRESSO calculations predict a small but complete gap of 200 meV and valence bands that are shifted to a lower energy compared to the KKR and FP-LMTO approaches. The FP-LMTO DOS calculations also reveal a band gap, albeit a smaller one, of 40 meV.

The discrepancy between the different approaches on the presence and size of the band gap could be due to several factors. Ultrasoft pseudopotentials are known to overestimate the magnetization energy in transition metals and this error is generally larger when the GGA is used.⁴⁶ Both the KKR and the FP-LMTO techniques are all-electron approaches so they avoid this problem. Another source of error could come from the calculation of the DOS in the KKR framework. The DOS

in this case can be expressed in terms of the system Green's function as

$$n(E) = \lim_{\eta \rightarrow 0^+} \left[-\frac{1}{\pi} \text{Im}G(E + i\eta) \right] \quad (1)$$

due to the fact that the Green's function is analytic everywhere in the complex plane except the real axis. In practical calculations, we add a small imaginary component, η , to the energy. This imaginary component leads to an artificial broadening of the DOS which can be expressed as a Lorentzian with a half-width of η . For the calculations shown in Fig. 7, an imaginary component of 1 meV was used. Broadening due to this source would be insufficient to explain the entire difference between the KKR and the FP-LMTO results. However, given that density functional calculations underestimate the experimental band gap, it is reasonable to assume that a perfect X-phase Cr_3Al crystal would be a small-band-gap semiconductor.

VII. DISCUSSION

Thus, the semiconductor-like behavior in Cr_3Al can be explained by X-phase-type chemical ordering and antiferromagnetism leading to a gap in the DOS. It is likely that a perfect crystal of X-phase Cr_3Al would be a true narrow-gap semiconductor with a band gap greater than 40 meV. Experimental estimations of the gap energy range from 10 to 95 meV.^{5,6,47,48} However, real samples thus far show the X phase occurring in very small domains presumably separated by antiphase boundaries.¹⁴ This disorder could smear the band edges or introduce defect states.⁴⁹ The experimental observations of Cr_3Al are consistent with a small but finite $\text{DOS}(E_F)$: the electronic contribution to the specific heat is nonzero, and the electrical resistivity increases with decreasing temperature algebraically rather than exponentially. This indicates either a semimetal (slightly overlapping flat bands at E_F) or a degenerate semiconductor (E_F just inside the band edge). The negative dependence of resistivity on temperature is most likely due to localization phenomenon or a rapidly varying $\text{DOS}(E_F)$, rather than true activated behavior.

A band gap can only occur in a material with an even number of valence electrons per unit cell in order to completely fill the valence band. So how can Cr_3Al , with 21 electrons per formula unit, have a band gap? The gap is possible because the primitive unit cell of the X phase, shown in Fig. 2(f), is actually Cr_6Al_2 , with a total of 42 valence electrons per unit cell. This aspect of the X-phase structure sets it apart from the other structures, which, although they may have a low $\text{DOS}(E_F)$, have an odd number of valence electrons per unit cell and therefore *must* have partially filled bands crossing E_F .

This study of the possible types of chemical ordering of Cr_3Al on the bcc lattice has important implications for materials design of transition metal compounds. It is clear from the calculated lattice constant and ferrimagnetic character of D0_3 Cr_3Al that the bulk samples reported in the literature and the thin-film samples reported here do not occur in the D0_3 structure. The energy calculations show that the D0_3 structure should not occur at all under equilibrium conditions. However, as shown in this paper with regard to C11_b Cr_3Al , nonequilibrium structures may occur for thin-film growth due to kinetics, surface energy effects, or epitaxy. Because there

are four other structures that are favored energetically (and, in some cases, entropically), it seems unlikely that the D0₃ structure could be formed. However, if D0₃ Cr₃Al were desired, for example, for study as a possible half-metal,¹² one direction of research would be to take advantage of the difference in lattice constant and grow ultrathin epitaxial films. The calculated D0₃ Cr₃Al lattice constant actually has an exceptionally good lattice match to MgO (0.1%) but has not appeared in any of the 400-Å thin films on MgO reported here. Growth of an ultrathin (unrelaxed) film may have more potential.

The Heusler structure (D0₃ for binary and L2₁ for ternary compounds) is fairly common, occurring for hundreds of transition metal–main group compounds. Cr₃Al, with X-phase ordering as the equilibrium state, is an exception to this scheme. This may represent a lower limit on the number of valence electrons in the unit cell for the Heusler structure to form. There are 21 valence electrons in the formula unit of Cr₃Al, while Heusler alloys are usually studied in the range of 22–31 valence electrons.³⁵ Thus, similar compounds containing transition metals from the left side of the periodic table should be studied for X-phase-type ordering like that seen in Cr₃Al.

VIII. CONCLUSION

In summary, we used both experimental thin-film growth methods and theoretical density functional theory calculations

to show how a combination of antiferromagnetism and X-phase chemical ordering leads to a gap in the band structure of Cr₃Al. Our experimental data correlate a transition from nonmetallic to metallic transport behavior around a 400 °C growth temperature, with the previously proposed structural phase transition (X phase → C11_b) occurring around the same temperature. Theoretically, the proposed X phase is found to be the lowest energy structure of those considered, implying that it should be the equilibrium structure occurring in nature. The commonly seen D0₃ (Heusler) structure is not observed and, based on calculations of total energy, is unlikely to occur. In light of these results, further characterization of the X-phase would be worthwhile.

ACKNOWLEDGMENTS

This work was supported by the US Department of Energy under Contract No. DE-AC02-05CH11231. Calculations were done at the Cornell Nanoscale Facility, part of the National Nanotechnology Infrastructure Network (NNIN), funded by the NSF. The authors would like to thank H. Akai for advice and insight on the AKAIKKR calculations, Mark van Schilf-gaarde for advice on the FP-LMTO calculations, and Cyrille Barreateau for providing the ultrasoft Cr pseudopotential used in this work.

*Corresponding author: zboekelheide@berkeley.edu; Present address: Material Measurement Laboratory, National Institute of Standards and Technology, Gaithersburg, Maryland 20899, USA

¹M. Weinert and R. E. Watson, *Phys. Rev. B* **58**, 9732 (1998).

²C. Uher, J. Yang, S. Hu, D. T. Morelli, and G. P. Meisner, *Phys. Rev. B* **59**, 8615 (1999).

³J. O. Sofo and G. D. Mahan, *Phys. Rev. B* **49**, 4565 (1994).

⁴J. Kübler, A. R. Williams, and C. B. Sommers, *Phys. Rev. B* **28**, 1745 (1983).

⁵Z. Boekelheide, A. X. Gray, C. Papp, B. Balke, D. A. Stewart, S. Ueda, K. Kobayashi, F. Hellman, and C. S. Fadley, *Phys. Rev. Lett.* **105**, 236404 (2010).

⁶D. J. Chakrabarti and P. A. Beck, *J. Phys. Chem. Solids* **32**, 1609 (1971).

⁷L. V. Nomerovannaya and V. A. Rassokhin, *Phys. Status Solidi A* **79**, 87 (1983).

⁸N. Pessall, K. P. Gupta, C. H. Cheng, and P. A. Beck, *J. Phys. Chem. Solids* **25**, 993 (1964).

⁹E. Fawcett, H. L. Alberts, V. Y. Galkin, D. R. Noakes, and J. V. Yakhmi, *Rev. Mod. Phys.* **66**, 25 (1994).

¹⁰W. Koster, E. Wachtel, and K. Grube, *Z. Metallkd.* **54**, 393 (1963).

¹¹A. Kallel and F. de Bergevin, *Solid State Comm.* **5**, 955 (1967).

¹²J. Li, H. Chen, Y. Li, Y. Xiao, and Z. Li, *J. Appl. Phys.* **105**, 083717 (2009).

¹³Z. Boekelheide, T. Saerbeck, A. P. J. Stampfl, R. A. Robinson, D. A. Stewart, and F. Hellman, *Phys. Rev. B* **85**, 094413 (2012).

¹⁴F. J. A. den Broeder, G. van Tendeloo, S. Amelinckx, J. Hornstra, R. de Ridder, J. van Landuyt, and H. J. van Daal, *Phys. Status Solidi A* **67**, 233 (1981).

¹⁵J. L. Murray, *J. Phase Equilib.* **19**, 367 (1998).

¹⁶M. Atoji, *J. Chem. Phys.* **43**, 222 (1965).

¹⁷T. J. Klemmer, V. R. Inturi, M. K. Minor, and J. A. Barnard, *Appl. Phys. Lett.* **70**, 2915 (1997).

¹⁸S. M. Zhou, K. Liu, and C. L. Chien, *J. Appl. Phys.* **87**, 6659 (2000).

¹⁹C. G. Lee, B. S. Kim, and K. Fukamichi, *IEEE Trans. Magn.* **35**, 2928 (1999).

²⁰P. J. Ozawa, S. Yoshizaki, S. Takeyama, T. Enjo, and K. Ikeuchi, *IEEE T. Compon. Hybr. CHMT-9*, 391 (1986).

²¹E. E. Fullerton, S. D. Bader, and J. L. Robertson, *Phys. Rev. Lett.* **77**, 1382 (1996).

²²E. E. Fullerton, K. T. Riggs, C. H. Sowers, S. D. Bader, and A. Berger, *Phys. Rev. Lett.* **75**, 330 (1995).

²³E. V. Kozlov, B. S. Semukhin, L. M. Rubinovich, and D. M. Shtern, *Fiz. Metal. Metalloved.* **56**, 547 (1983).

²⁴<http://kkk.phys.sci.osaka-u.ac.jp/>.

²⁵J. Koringa, *Physica* **13**, 392 (1947).

²⁶W. Kohn and N. Rostoker, *Phys. Rev.* **94**, 1111 (1954).

²⁷P. Soven, *Phys. Rev.* **156**, 809 (1967).

²⁸H. Akai, *J. Phys.: Condens. Matter* **1**, 8045 (1989).

²⁹J. P. Perdew, J. A. Chevary, S. H. Vosko, K. A. Jackson, M. R. Pederson, D. J. Singh, and C. Fiolhais, *Phys. Rev. B* **46**, 6671 (1992).

³⁰P. Giannozzi *et al.*, *J. Phys.: Condens. Matter* **21**, 395502 (2009).

³¹M. Methfessel, M. van Schilf-gaarde, and R. A. Casali, in *Electronic Structure and Physical Properties of Solids: The Uses of the LMTO Method*, Lecture Notes in Physics, Vol. 535, edited by H. Dreysse (Springer-Verlag, Berlin, 2000).

- ³²J. P. Perdew, K. Burke, and M. Ernzerhof, *Phys. Rev. Lett.* **77**, 3865 (1996).
- ³³R. Soulaïrol, C.-C. Fu, and C. Barreteau, *J. Phys.: Condens. Matter* **22**, 295502 (2010).
- ³⁴R. Hafner, D. Spišák, R. Lorenz, and J. Hafner, *Phys. Rev. B* **65**, 184432 (2002).
- ³⁵I. Galanakis, K. Özdoğan, E. Şaşıoğlu, and B. Aktaş, *Phys. Status Solidi A* **205**, 1036 (2008).
- ³⁶D. W. Cooke, Z. Boekelheide, D. R. Queen, and F. Hellman, *J. Appl. Phys.* **105**, 07C314 (2009).
- ³⁷D. W. Cooke, Ph.D. thesis, University of California, Berkeley (2010).
- ³⁸F. Heiniger, E. Bucher, and J. Muller, *Phys. Kondens. Mater.* **5**, 243 (1966).
- ³⁹D. G. Laurent, J. Callaway, J. L. Fry, and N. E. Brener, *Phys. Rev. B* **23**, 4977 (1981).
- ⁴⁰J. F. Goff, *Phys. Rev. B* **4**, 1121 (1971).
- ⁴¹W. L. McMillan, *Phys. Rev.* **167**, 331 (1968).
- ⁴²S. D. Brorson, A. Kazeroonian, J. S. Moodera, D. W. Face, T. K. Cheng, E. P. Ippen, M. S. Dresselhaus, and G. Dresselhaus, *Phys. Rev. Lett.* **64**, 2172 (1990).
- ⁴³P. B. Allen, *Phys. Rev. B* **36**, 2920 (1987).
- ⁴⁴E. Fawcett, *Rev. Mod. Phys.* **60**, 209 (1988).
- ⁴⁵R. M. Martin, *Electronic Structure: Basic Theory and Practical Methods* (Cambridge University Press, Cambridge, 2005).
- ⁴⁶G. Kresse and D. Joubert, *Phys. Rev. B* **59**, 1758 (1999).
- ⁴⁷M. A. Lind and J. L. Stanford, *J. Phys. Soc. Jpn.* **53**, 4029 (1984).
- ⁴⁸Our photoemission study showed the valence band edge 95 meV below E_F , measured at room temperature. For comparison, the density functional theory calculations are made at 0 K.
- ⁴⁹D. I. Bilc and P. Ghosez, *Phys. Rev. B* **83**, 205204 (2011).
- ⁵⁰W. Koster, E. Wachtel, and K. Grube, *Al-Cr Phase Diagram*, *ASM Alloy Phase Diagrams Center*, edited by P. Villars (ASM International, Materials Park, OH, 2006); [<http://www1.asminternational.org/AsmEnterprise/APD>].
- ⁵¹J. L. Murray, *Al-Cr Phase Diagram*, *ASM Alloy Phase Diagrams Center*, edited by P. Villars (ASM International, Materials Park, OH, 2006); [<http://www1.asminternational.org/AsmEnterprise/APD>].